Environmental Science Nano

Sunlight-driven atmospheric water capture capacity is enhanced by nano-enabled photothermal desiccants

Journal:	*Environmental Science: Nano*
Manuscript ID	EN-ART-05-2020-000463.R1
Article Type:	Paper

Solar desiccant driven atmospheric water capture can provide access to drinking water off the water- and energy- grids. Sunlight-driven direct atmospheric water capture using nano-enabled photothermal desiccants can be applied in semi-arid and humid climates to produce >2 L H_2O/m^2/day. Nanomaterials provide surface heating of the desiccants to desorb water vapor. Nano-enabled photothermal desiccants produce more water than traditional desiccants.

Sunlight-driven atmospheric water capture capacity is enhanced by nano-enabled photothermal desiccants

Anjali Mulchandani, Shannon Malinda, Justin Edberg, and Paul Westerhoff*

School of Sustainable Engineering and the Built Environment, Arizona State University, Tempe, AZ, 85008-3005, USA

NSF Nanosystems Engineering Research Center for Nanotechnology-Enabled Water Treatment

Article submitted to Environmental Science: Nanotechnology

*Corresponding author:

Email: p.westerhoff@asu.edu

Phone: 480-965-2885

Abstract

Atmospheric water capture (AWC) is an alternative method of localized water production whereby water vapor is removed from air to produce drinking water. The most advantageous AWC applications are for developing solar energy driven, off-grid water sources. Solid phase silica gel (SiO_2) desiccant materials can adsorb and concentrate water vapor in many relative humidity (RH) (20–100%) and temperature (20–40°C) conditions. Generating sufficient solar thermal heat to release of all the sorbed water vapor from the desiccant bed can take many hours of sunlight, which limits the AWC system to just one adsorption-desorption-condensation cycle per day. In this work, we applied solar-light active photothermal nanomaterials (gold cubes and rods, carbon black) on SiO_2 desiccant surfaces with the aim of providing localized heat sources, thereby rapidly increasing desiccant surface temperature, improving kinetics and totality of water vapor desorption, and allowing additional AWC cycles per day. Desiccants were tested for adsorption at 40%, 60%, and 80% RH and desorption under 1-Sun simulated solar irradiation. In the optimal use-case scenario, 5wt% carbon black coated SiO_2 could cycle through >10 adsorption-desorption phases per day to produce 0.47 gH_2O/g desiccant/12 hours (2 L/m^2) at 40% RH. By innovating material and AWC system design to operate over multiple atmospheric water harvesting cycles per day, we showed that nano-enabled photothermal desiccants can be applied in semi-arid climates to produce 10-fold more water than one standard cycle using a bare SiO_2 desiccant.

Keywords

Atmospheric water harvesting, decentralized, thermal regeneration

Introduction

Removing pollutants and salts from conventional (e.g., lakes, rivers, groundwater) or unconventional water supplies (e.g., oceans, brackish groundwater, wastewater, stormwater) and distributing clean water within rural or decentralized communities can be energy intensive, costly, and produce large amounts of waste residual.[1–7] Atmospheric water capture (AWC) is an emerging method of decentralized water production whereby very low salt content water is removed from air without producing concentrated waste streams. As a hydrologic reservoir, the atmosphere contains 12,900 km^3 of water, ~14% of the freshwater volume stored in lakes and rivers combined.[8] Its universal presence suggests that atmospheric water vapor could be used in many locations. Among the most interesting AWC applications is to enable an off-grid water source (i.e., away from both the municipal water and electricity grids) for use in rural homes, mobile military outposts, or in disaster relief scenarios where the cost or time to build fixed infrastructure is a major barrier.

Devices that harvest water from the air can be grouped as: 1) dew collectors, 2) dew point condensation dehumidifiers, and 3) relative humidity (RH) capture by adsorption-desorption cycling (i.e., desiccants).[9,10] Dew collection is only relevant for fully-saturated air such as fog, where RH is >100%.[11–16] Dehumidifying condensation systems often utilize electrically-powered compressors that use refrigerants to directly cool humid air to below the dew point temperature. This process is only effective for higher RH (at least >30–40%) and is energy intensive (0.5–2 kWh / L water produced). [10,17–24]

Desiccant-based AWC can use liquid desiccants (e.g., $CaCl_2$), solid desiccants (e.g., silica gel, zeolites, metal organic frameworks (MOFs)), or super moisture-adsorbent gels (SMAGs) to capture water vapor from the air.[25–27] The quantity of water captured by desiccant-based AWC is

a function of RH, wherein the vapor pressure differential between the air and the desiccant surface acts as a driving force for sorption.[26] Heat is applied to drive desorption of vapor from the desiccant onto a cool surface where clean water condenses and can be collected. Many designs exist to operate desiccants in continuous flow modes (e.g., packed bed, fluidized bed), and water is collected using a simple heat exchanger.[28–37]

Liquid desiccants react with water vapor to form a complexed hydrate (e.g., $CaCl_2 \cdot H_2O$) that continues to absorb water and produces saturated salt solutions. Eventually the salt and water must be separated by heat to obtain fresh water and regenerate the desiccant for reuse.[34,38] Liquid desiccants can produce large water volumes (up to 2 g H_2O/ g desiccant), but the AWC process requires three phase changes: from water vapor to liquid salt, to saturated water vapor, to re-condensed and low-salt liquid water. In contrast, solid desiccant systems only undergo one phase change. First, water vapor adsorbs to solid desiccants; it does not change state on the surface.[39] Second, nearly-saturated water vapor desorbs from the desiccant using heat. Third, liquid water is condensed from the high RH air on a cool surface. Because dew collectors and dew point condensation are ineffective in many climates,[40–42] and because of the complexity and multiple state changes required for salt-based desiccants, this work focused on solid desiccants for AWC.

Desiccant-based AWC systems often operate by adsorbing water vapor at night, when RH is high,[43] and utilize solar heating during the day to desorb vapor and condense it to produce drinkable water.[40,41,44–46] Solar heat is a free, off-grid energy source. Existing literature focuses on materials that achieve high water vapor adsorption capacity (e.g., 1.2 g H_2O / g MOF MIL101(Cr) at 80% RH [47–49]). Less attention has been given to the energy and rate of water vapor desorption, which can limit the overall water production capacity of AWC systems that

rely on solar heating. The temperature required to heat the desiccants for desorption (>90°C for SiO_2, >150°C for zeolite, >85°C for MOFs) limits AWC. Generating sufficient solar thermal heat to release all the sorbed water vapor from the desiccant bed can take many hours of sunlight, which limits the AWC system to just one adsorption-desorption-condensation cycle per day. Thus, in systems with large masses of super-efficient water sorption capacities (e.g., >1g water / g sorbent), solar heating may limit the potential of AWC systems.

Given that available solar thermal energy is a limiting factor, there is a need to develop novel desiccant materials that either require less thermal heat input or can maximize the available solar thermal energy to achieve complete desorption. Broad-wavelength light-absorbing photothermal nanomaterials convert photons from incident solar radiation into localized heat. Photothermal nanoparticles such as gold and carbon black have been applied to heat membranes in nanophotonics-enabled solar membrane distillation[50] and inactivate microbes in solution and on surfaces.[51] In this work, we applied solar-light active photothermal nanomaterials (gold cubes and rods, carbon black) on silica gel (SiO_2) desiccant surfaces with the aim of providing localized heat sources, thereby rapidly increasing desiccant surface temperature and improving kinetics of water vapor desorption and desiccant regeneration. Faster desiccant regeneration can lead to multiple AWC cycles per day. [52,53]

Gold nanoparticles (AuNPs) are both plasmonic and photothermal; when light at the surface plasmonic resonance (SPR) wavelength hits the nanoparticle (NP), the electrons in the NP's conduction band are excited and begin to oscillate, creating a hot electron distribution. The electron oscillation decays by transferring the generated heat to the surrounding media.[54–59] The NP size and shape can have a large impact on the SPR wavelength(s) and, correspondingly, the SPR induced photothermal heating.[60] Gold nanorods (AuNR) have two SPR peaks (520nm,

790nm), indicating they can use more photons from the solar spectrum than gold nanocubes (AuNC, SPR peak 534 nm) to generate heat. [51,61] To contrast narrow spectral properties of AuNPs, we compared them to a lower cost and broadband spectrum absorbing, commercially available carbon black (CB) NPs. [50,51,60,62,63]

The goal of this study was to understand material properties that can maximize the net water volume that desiccants can capture during the day. The net water production is a function of the water capacity during one adsorption-desorption cycle multiplied by the number of cycles performed per day. The number of cycles that can be operated per day depends on the water vapor adsorption and desorption rates via the desiccants' solar photothermal heating capacity. Photothermal nanomaterials (AuNC, AuNR, CB) were chemically attached to micron-sized silica gel desiccants to increase desiccant surface temperature under sunlight, increase water vapor desorption rate, and facilitate multiple cycles of water capture throughout a 12-hour day period. Material characterizations of nano-enabled desiccants were related to their photothermal properties under simulated 1-Sun solar radiation. This work is among the first to perform atmospheric water capture experiments in multiple realistic environmental conditions (40%, 60%, and 80% RH) to determine optimal use-case for nano-enabled photothermal desiccants.

Materials and Methods

Synthesis of nano-enabled photothermal desiccants

Silica gel desiccants (high purity grade, pore size 40Å, 70–230 mesh particle size (63–210 μm), (3-Aminopropyl) triethoxysilane (APTES), hexadecyltrimethylammonium bromide (CTAB), gold (III) chloride hydrate ($HAuCl_4$), sodium borohydride ($NaBH_4$), ascorbic acid, silver nitrate ($AgNO_3$), and ethanol were acquired from Sigma Aldrich. ACS-grade hydrochloric

acid (HCl) was obtained from VWR. Ultrapure water (18.2 MΩ cm, Barnstead GenPure xCAD Plus) was used to make all solutions.

Silica gel desiccants (SiO_2) with pore size 40 Å and mesh particle size 70–230 (63–210 μm) were selected because they have the highest reported surface area among commercial silica gel desiccants (500 m^2/g), and surface area is a driving property in maximizing water vapor adsorption.[43] SiO_2 was washed with ultrapure water and separated using centrifugation (5000 RPM, 30 min) two times and washed and centrifuged once with ethanol. Washed SiO_2 (20 g) was silanized with 2.14 mmol APTES per gram SiO_2 via reflux condensation in 400 mL ethanol for 12 hours at 80°C. SiO_2-APTES was washed with ethanol and collected after vacuum filtration using 0.45 μm nylon filter, then dried overnight at 80°C. APTES is bound to the SiO_2 via the formation of Si–O–Si bonds with surface silanol groups. [64–68] The APTES amine terminus ($–NH_2$) faces outwards to covalently bond with gold or carbon. [51,69–72]

AuNC and AuNR were synthesized using a seeded-growth method and capped with CTAB (details provided in S.I.). The AuNC solution is a bright red color with concentration 25 mg/L and SPR peak at 534 nm. The AuNR solution is a deep purple color with concentration 80 mg/L and has two SPR peaks at 520 nm and 790 nm. CB NPs were purchased in powder form (Emperor 2000 from Cabot Corporation) and used without further purification.

For preliminary photonic and photothermal experiments, six NP mass loadings (0.1–10 wt% NP/SiO_2) were prepared for each NP. Varying volumes of premade 25 mg/L AuNC or 80 mg/L AuNR solution were added to 0.2 g premade SiO_2-APTES in Qorpak 500 mL wide mouth amber bottles to produce mass loadings of 0.1–7 wt% AuNP-SiO_2. Nanopure water was added to each bottle such that the final volume in each bottle was 400 mL. To synthesize CB-SiO_2, various masses of commercial CB were added to 0.2 g SiO_2-APTES and 400 mL water in

Qorpak 500 mL wide mouth amber bottles to produce mass loadings of 0.1–10 wt% CB-SiO_2. Secondary water capture experiments required triplicate production of 1 g 5wt% NP-SiO_2: 1 g of premade SiO_2-APTES was added to either 625 mL of AuNC (2 L of 25 mg/L AuNC were pre-concentrated by centrifuging and resuspending in 625 mL water), 625 mL 80 mg/L AuNR solution, or 50 mg CB and 625 mL water in Qoropak 1250 mL wide mouth amber bottles. Amber bottles were placed on a rotating shaker table (350 RPM). After mixing the SiO_2-APTES with NPs overnight, the desiccants settled for 2 hours, then the supernatant was removed. The jars with wet desiccants were dried overnight in an oven at 105°C. Dry desiccants were collected and stored in glass vials at room temperature until use. **Figure 1** shows the desiccants (NP-SiO_2), which varied in color depending on mass loading from various shades of greys for the CB on SiO_2-APTES (CB-SiO_2), pinks for AuNC on SiO_2-APTES (AuNC-SiO_2), and blues for AuNR on SiO_2-APTES (AuNR-SiO_2).

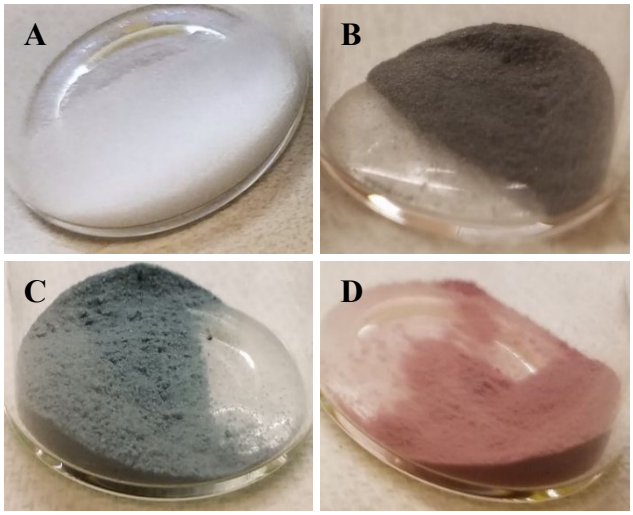

Figure 1: A) Bare SiO_2 desiccants. **B)** 5wt% carbon black coated SiO_2 desiccants. **C)** 5wt% gold nanorod coated SiO_2 desiccants. **D)** 5wt% gold nanocube coated SiO_2 desiccants.

The bare SiO_2 desiccants had an average spherical diameter of 136 μm, which equates to $5.8x10^{-8}$ m^2 of external surface area for attaching APTES and NPs. **Figure S1** shows TEM images of the AuNPs. SiO_2 pores were 4 nm (40 Å), while AuNR were 20 nm x 60 nm and AuNC had unit length 60 nm. Dynamic light scattering measurement of CB NPs showed they had a hydrodynamic diameter of 160 nm.[51] NP dimensions were used to calculate surface loadings. A 2.2wt% loading of AuNC on SiO_2 is the equivalent of a monolayer, or 100% surface coverage. For AuNR, 0.6wt% loading is a monolayer, and for CB, 0.3wt% loading is a monolayer. NP mass loadings of 0–7 wt% for AuNC, 0–7 wt% for AuNR, 0–10 wt% for CB were prepared to ensure complete coverage of the SiO_2 desiccant with NPs and to test if additional layers of NP had impact on photothermal properties. Brunauer-Emmet-Teller (BET) surface area measurement of desiccants was conducted using Micromeritics TriStar II 2030 instrument. Supplemental information provides sample preparation and methodology details for TEM and BET.

UV-Visible light absorption by nano-enabled photothermal desiccants

Diffuse reflectance spectra of the desiccants were measured using Perkin Elmer Lambda 18 UV-Vis Spectrometer with 150 mm integrating sphere. Diffuse reflectance measures the portion of incident light in a spectrometer that enters the voids of the powders, scatters, and is not absorbed. Diffuse reflectance spectroscopy has been proven to accurately correlate with localized light absorption for both carbon and gold nano-enabled solid substrates. [50,51,73,74]

The Kubelka-Munk function ($F(R)$) (**Equation 1**) converts reflectance measurements (R) to a ratio of absorption (K) to scattering (s) coefficients, assuming a uniform, infinitely thick layer of material that either absorbs or scatters radiation.[75]

$$F(R) = \frac{(1-R)^2}{2R} = K/s \quad (1)$$

K/s values above unity indicate absorption is more dominant than scattering, *K/s* values equal to 1 indicate equivalent absorption and scattering, and *K/s* values less than unity mean scattering is dominant.

Nano-enabled photothermal desiccant heating under simulated solar irradiation

Desiccant (0.03 g) was mounted onto a glass microscope slide (Fisherbrand, thickness 1 mm) using a 25 mm x 25 mm square of Scotch double-sided tape. The slide was placed perpendicular to the horizontal path of light from a Newport 1000 W Hg/Xe lamp at a distance where radiation intensity was 1000 W/m^2 (1-Sun). An infrared temperature sensor (Omega, OS-MINIUSB) was placed directly above the sample, and sample temperature was recorded at 1 second intervals. Samples were irradiated until stable maximum temperature was reached. Then the light source was covered to allow samples to cool. Heating experiments for each desiccant were performed in triplicate.

Water vapor adsorption onto nano-enabled photothermal desiccants under controlled humidity

Water vapor adsorption experiments were performed in a 0.16 m^3 polycarbonate enclosure (**Figure S2**). The enclosure contained 2 balances (Ohaus Pioneer PX224AM, readability 0.0001 g), an ultrasonic humidifier with hose attachment (Electro-Tech Systems model 5462), a circulation fan (Vornado Flippi V6), and a combined humidity and temperature meter (Omega RH820U). The humidifier tube attachment was placed above the fan to evenly distribute humid air throughout the chamber. Humidity and temperature were monitored and logged by the meter every second. Experiments were performed at ambient temperature (20–22°C), and RH was maintained at either 40%, 60%, or 80% (+/- 2%) by manually adjusting the

humidifier throughout the experiment duration. One gram of 5wt% NP-SiO_2 dry desiccant (removed from oven at 105°C immediately before experiment) was placed on a balance in an open glass petri dish, and weight increase due to water vapor adsorption was recorded by Ohaus serial port data collection software every 5 seconds.

Water vapor desorption off nano-enabled photothermal desiccants under simulated solar irradiation

Water vapor desorption tests were performed in ambient lab environment (RH 25%, Temperature 20°C). After saturating the desiccant in the humidity-controlled enclosure (**Figure S2**), the glass petri dish containing saturated desiccant was placed on a balance beneath a vertical beam from Newport 1000 W Hg/Xe lamp with A.M. 1.5G filter at a distance where radiation intensity was equivalent to 1-Sun (1000 W/m^2) (**Figure S3**). Mass loss over time as attributed to water vapor desorption was recorded at 5 second intervals from the balance using a serial port and data collection software (Ohaus). Two-tailed t-tests were performed on adsorption and desorption data obtained by triplicates of desiccant samples to determine statistical similarity (see S.I. for details).

Results and Discussion

Photonic characterization of NPs and nano-enabled photothermal desiccants

AuNC, AuNR, and CB NPs exhibited light absorption properties both dispersed in water and attached on desiccant surfaces. In water, the AuNR showed SPR peaks at 520 nm and 790 nm, and AuNC showed a peak at 534 nm. CB exhibited broad absorption through the visible and near-IR wavelength spectra (**Figure S4A**). **Figure 2** shows the Kubelka-Munk transformation of diffuse reflectance for the SiO_2 desiccants with and without a 1wt% and 5wt% NP mass loading

on their surface. As anticipated, there were similarities in the spectral shape from NPs in water to Kubelka-Munk transformations of NP-SiO_2 solids. [50,51]

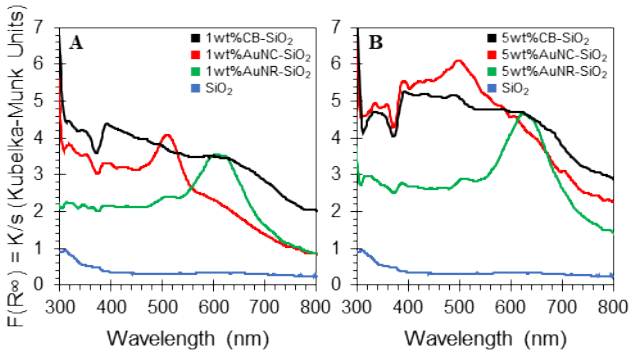

Figure 2: Kubelka-Munk transformation of diffuse reflectance on **A)** 1wt% or **B)** 5wt% nanoparticle-loaded SiO_2 .

The magnitude of wavelength of light absorption by the NPs shifts when attached to SiO_2. It was hypothesized that the magnitude of light absorption by the desiccants would follow the trend CB-SiO_2 > AuNR-SiO_2 > AuNC-SiO_2 because this was the trend seen for NPs in solution. (**Figure S4A**) However, **Figure 2** shows for both the 1wt% and 5wt% NP-SiO_2 the light absorption trend is CB-SiO_2 = AuNC-SiO_2 > AuNR-SiO_2. Higher absorbance by AuNC-SiO_2 compared to AuNR-SiO_2 was not because a higher NP density attached to the SiO_2. In fact, based on the NP size and density, a 5wt% loading of AuNPs is equivalent to 230% surface coverage for AuNC and 830% surface coverage for AuNR. Instead, it is likely that the combination of the arrangement of nanorods on the SiO_2 substrate surface and the incident direction of light interacting with the nanoparticles led to a damping or suppression of the plasmonic resonance and higher light scattering.[76,77]

The plasmonic resonance peaks of AuNPs (both cubes and rods) exhibited a blue-shift from measurements in water vs air. The SPR peaks for AuNR in solution were at 520 nm and 790 nm, while the SPR peaks for AuNR-SiO_2 were at 505 nm and 625 nm. The SPR peak for AuNC in solution was at 534 nm and shifted to 500 nm for AuNC-SiO_2. The refractive index (RI) of water (1.33) is higher than that of air (1.0), [78] which causes the nanoparticle extinction spectrum to shift when the particles are transferred from a water matrix to air. This is important because solar irradiance is higher at the blue-shifted wavelengths (1.40 W/m^2 at 625 nm, 1.56 W/m^2 at 505 nm) compared with the anticipated absorption wavelengths (1.09 W/m^2 at 790 nm, 1.53 W/m^2 at both 534 nm and 520 nm). Therefore, the blue-shift should not have a detrimental impact on light absorption and corresponding heat production by AuNP-SiO_2 under exposure to solar irradiation in air.

Comparing the 1wt% and 5wt% NP loadings shows that higher surface NP loading increased the light absorption. However, above 5wt% loadings, absorption plateaued at an "absorption maxima", indicating any further NP loading will not further enhance light absorption (**Figure S5**). Therefore, AWC analysis was performed on 5wt% NP-SiO_2 because additional mass loadings were unlikely to lead to additional heating potential but likely to reduce water vapor mass transport rates at the desiccant surface.

Photothermal characterization of nano-enabled photothermal desiccants under simulated solar irradiation

Attachment of photothermal NPs to desiccant surfaces increased the desiccant surface temperature under simulated solar irradiation. For each of the three NPs, higher NP surface loading always increased the rate and maximum temperature. **Figure 3A** shows CB loading of 1wt% achieved similar maximum surface temperature as 2.5, 5, and 10wt%. Maximum surface

temperature and heating rate of 5wt% and 10% CB was statistically similar ($p>0.6$). For the same simulated solar experiments and 5wt% NP mass loadings, **Figure 3B** shows CB achieved a higher maximum surface temperature (59°C) than either AuNC-SiO_2 (41°C), AuNR-SiO_2 (31°C), or the un-modified bare SiO_2 (28°C). The heating rate (°C/min) was calculated as the slope of the first minute of temperature versus time shown in **Figure 3**. Calculated heating rates are summarized in **Table 1.** At 5wt% NP-SiO_2 loading, the CB heating rate was 2 times faster than AuNC and 4 times faster than AuNR-SiO_2. We concluded that AuNC-SiO_2 heated more slowly and to a lower temperature than CB-SiO_2 because, even though the integrated Kubelka-Munk absorbance are near equal, there is energy lost in the conversion of SPR electron oscillation to heat. [60]

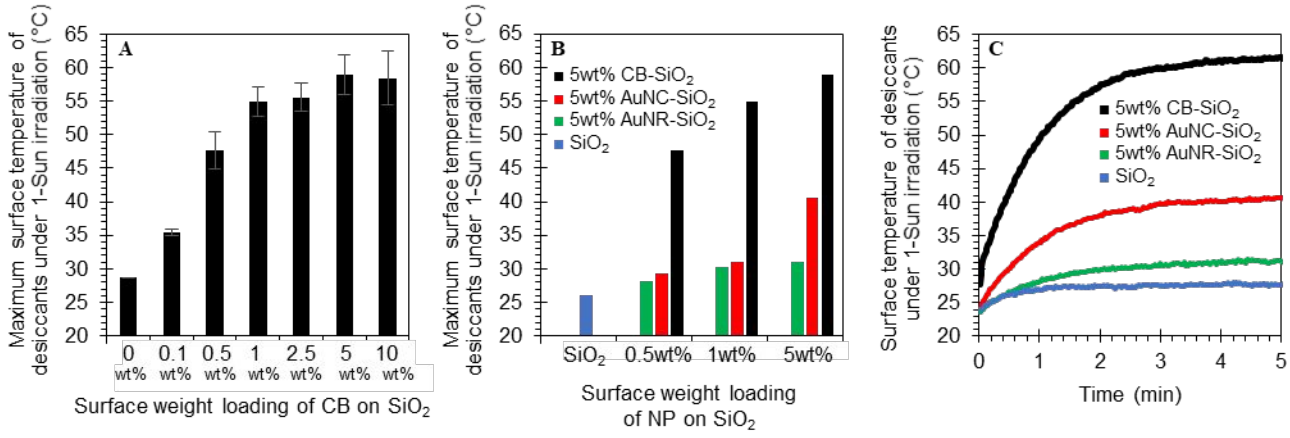

Figure 3: Dry desiccant surface temperature under 1-Sun solar irradiation. **A)** Maximum surface temperature of carbon black loading on SiO_2 desiccants. **B)** Maximum surface temperature of various NP loadings on SiO_2. **C)** Change in 5wt% NP-SiO_2 desiccant surface temperature over time.

Table 1: Heating rate and maximum surface temperature of 0.03 g desiccant sample attached to a glass slide and placed perpendicular to the beam path of 1-sun irradiation

Loading (wt%NP-SiO_2)	Carbon Black		Gold Nanocube		Gold Nanorod	
	Heating Rate (°C/min)	Max Temperature (°C)	Heating Rate (°C/min)	Max Temperature (°C)	Heating Rate (°C/min)	Max Temperature (°C)
0	2.3	28.2	2.3	28.2	2.3	28.2
0.25	12.5	47.6	2.4	28.8	2.2	28.5
0.5	12.3	49.4	3.0	29.5	2.6	30.2
1	14.5	52.7	4.2	31.2	3.5	30.4
2.5	15.5	52.9	6.9	35.8	4.4	31.9
5	18.8	59.0	9.5	40.7	4.3	31.4
7	--	--	7.7	38	5.3	33.6
10	19.2	58.1	--	--	--	--

Water vapor adsorption onto desiccants under variable humidity conditions

As illustrated for representative samples in **Figure 4**, water harvesting experiments were conducted in two phases. First, water vapor was adsorbed, and experiments run for 15 to 60 minutes past achieving a saturation plateau to confirm maximum adsorption. Second, water vapor desorption was initiated and run until a second plateau was achieved. Water vapor capture experiments were performed on 5wt% NP-SiO_2 because they had optimal heating rates and maximum surface temperatures (**Table 1**). Maximum water vapor adsorption rates and capacities were determined at three RH values (40, 60, 80%) for the bare SiO_2 and the 5wt% NP-SiO_2. **Figure 4A** shows that for 40% RH all desiccants were saturated with water vapor within ~45 minutes. The time required to achieve water vapor saturation increased with increased RH. At 60% RH, all desiccants reached their maximum sorption capacity within 1 hour (**Figure 4B**), and at 80% RH, all desiccants reached maximum sorption capacity in 8 hours (**Figure 4C**).

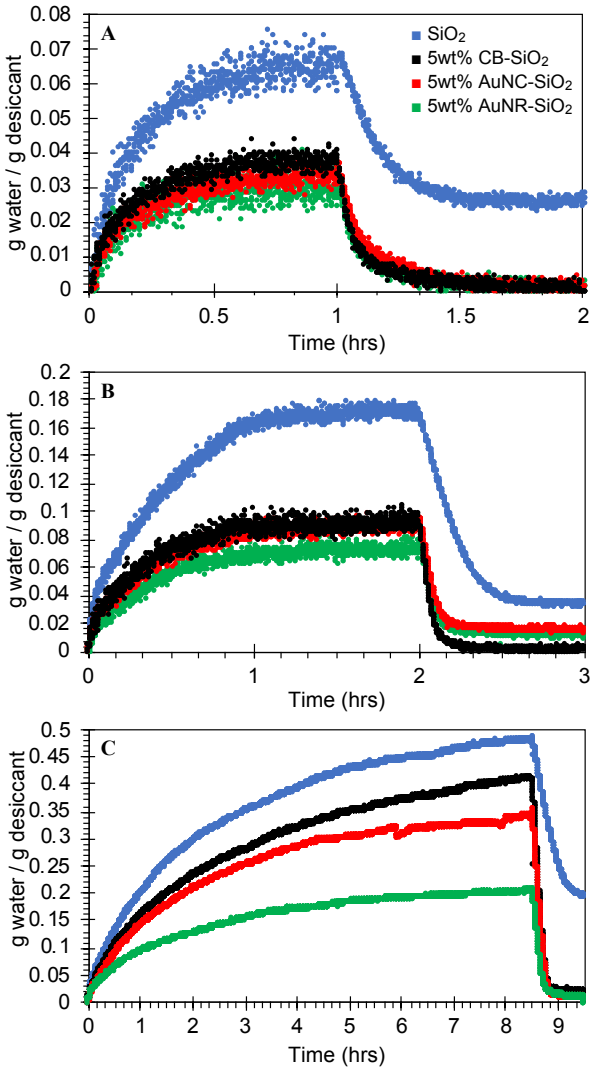

Figure 4: Water harvesting experiments conducted for bare SiO_2, 5wt%CB-SiO_2, 5wt%AuNC-SiO_2, and 5wt%AuNR-SiO_2. Water vapor adsorption under controlled humidity conditions and desorption under 1-sun irradiation over time. Adsorption experiments performed at **A)** RH = 40%, **B)** RH = 60%, **C)** RH = 80%.

Table S1 summarizes maximum adsorption capacities for all experiments, which at 40% RH ranged from 0.045 ± 0.0036 to 0.067 ± 0.0033 gH_2O/g desiccant. The bare SiO_2 desiccant adsorbed more water vapor ($p<0.03$) than either of the three NP enabled desiccants. Among the three NP-enabled desiccants, the maximum water adsorption capacities were statistically similar ($p>0.25$).

A similar trend was seen for adsorption experiments at 60% RH. Silica gel desiccants adsorbed 0.201 ± 0.0152 gH_2O/g desiccant within 1 hour, which is nearly double the capacity of all NP-SiO_2 ($p<0.003$). At 80% RH, the time required for water vapor saturation of the desiccants increased to 6–8 hours. Maximum sorption capacities of SiO_2 (0.495 ± 0.0284) and 5wt% CB-SiO_2 (0.421 ± 0..643) were statistically similar ($p=0.143$), as were the sorption capacities of 5wt% CB-SiO_2 and 5wt% AuNC-SiO_2 (0.352 ± 0.0250, $p=0.185$).

Two factors may be leading to lower adsorption of NP-enabled desiccants compared with bare desiccants. First, the APTES coating may be blocking desiccant pores. Second, NPs may be hindering access to the desiccant pores. The measured BET surface area for bare SiO_2 desiccant was 459.2 m^2/g. Treating SiO_2 with the APTES linker alone decreased the surface area by 37% to 290 m^2/g. Attachment of CB or AuNC to SiO_2-APTES did not impact the surface area beyond APTES treatment alone (**Table S2**), whereas AuNRs decreased the available surface area by 46% relative to the bare silica desiccant. Decrease in surface area limits sites where water vapor can adsorb.[43] Thus, the APTES treatment is responsible for the lower water vapor adsorption for NP-SiO_2 relative to bare SiO_2 (**Figure 4**), and future work should focus on linkers that have a smaller effect on NP-SiO_2 surface area.

Water vapor desorption from desiccants under simulated solar irradiation

After saturation was achieved, water vapor desorption was monitored for at least 1 hour under 1-Sun simulated solar irradiation. Desorption rates (gH_2O/min) were calculated as the slope of mass change over time for the first 5 minutes and are summarized in **Table S1** for all experimental conditions. **Figure 4A** shows one adsorption-desorption cycle for selected desiccants. Faster desorption rates were achieved by NP-SiO_2 than for bare SiO_2, which is attributed to higher surface temperatures (**Figure 3**). Notably, CB-SiO_2 achieved a surface temperature 20–30°C higher than bare SiO_2 for all RH conditions and consequently achieved nearly double the desorption rate. In plotting results from all the data together, there was a clear trend between higher NP-SiO_2 surface temperatures and water vapor desorption rate (**Figure S6**). The higher variability obtained in 80% RH desorption experiments was likely due to multi-layer desorption, with water vapor leaving the surface of the desiccant faster than water vapor bound in the pores. NP-SiO_2 achieved near complete water desorption during the heating cycle whereas 40% of the water vapor failed to desorb from the bare SiO_2 because it did not achieve a high enough temperature.

In all cases, **Figure 5A** shows that more water was produced (i.e., harvestable) after desorption from higher RH exposures for any given desiccant. Water harvested at 40% RH by SiO_2 and all NP-SiO_2 in one adsorption-desorption cycle was statistically similar. However, **Figure 5A** also shows that during any one water vapor cycle at 60% or 80% RH, the bare SiO_2 produced more water than any of the NP-SiO_2; the lower water vapor mass adsorption was due to APTES blockage of desiccant pores in NP-SiO_2. Only at 80% RH did one NP-SiO_2 (5wt% CB-SiO_2) yield a similar quantity of harvestable water to the bare SiO_2. Thus, if only one adsorption-

desorption cycle per day was conducted, there would be limited benefit of nano-enabling the SiO_2 desiccant.

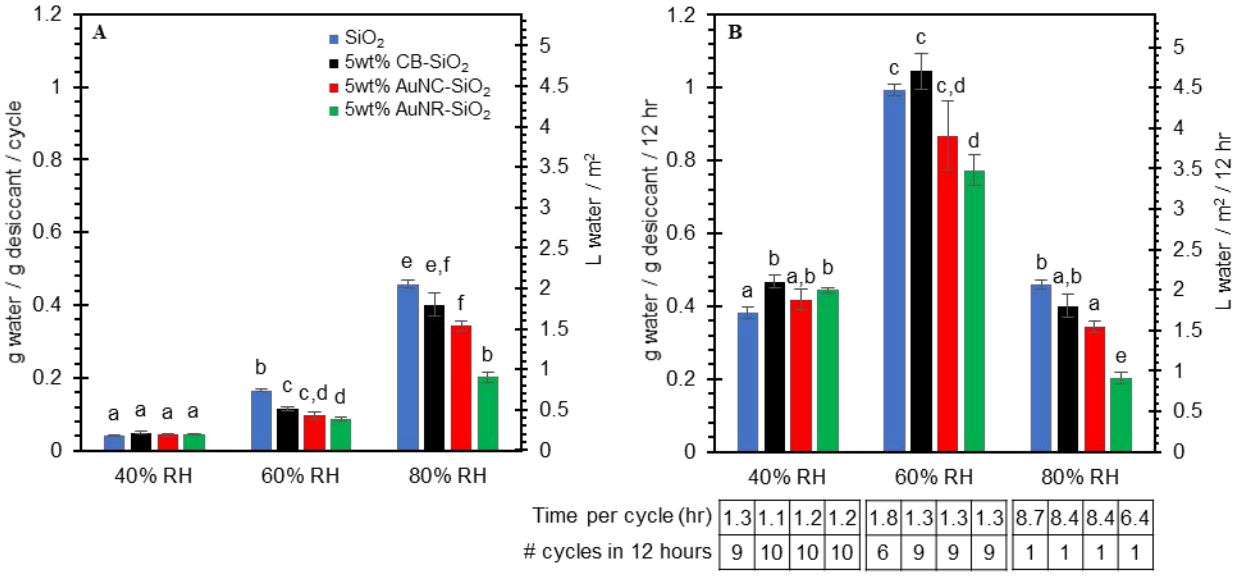

Figure 5: A) Water volume captured per gram desiccant for one adsorption-desorption cycle (experimental). **B)** Water volume captured per gram desiccant for multiple cycles over 12 hours (theoretical). Time per cycle combines adsorption and desorption time.

Operating multiple adsorption-desorption cycles with nano-enabled photothermal desiccants

Considering that the volume of water captured by bare SiO_2 and all NP-SiO_2 at 40% RH was statistically equal and all NP-SiO_2 had faster desorption rates, we hypothesized NP-SiO_2 could perform more adsorption and desorption cycles over a 12-hour daylight period to yield a higher water volume. Accordingly, multiple sequential adsorption-desorption cycles were conducted over a 12-hour period to estimate net water harvest capacity and to evaluate material stability. In these experiments, as soon as the desiccant achieved saturation it was subjected to a desorption cycle. **Figure 6** shows representative data at 40% RH for bare SiO_2 and the best-performing NP-SiO_2 (5wt%CB-SiO_2). As illustrated by near identical rates and extents of water

vapor adsorption and desorption, both the bare desiccants and NP-SiO_2 performed consistently over multiple cycles. As shown in **Figure 6a**, the NP-SiO_2 achieved 11 complete adsorption-desorption cycles within 12 hours, with complete desorption of water vapor (e.g., **Figure 4a**) in each cycle, yielding 0.562 g H_2O/g desiccant. In parallel experiments (**Figure 6b**), the SiO_2 desiccant only achieved 9 cycles within 12 hours, and only yielded 0.460 g H_2O/g desiccant because of its slower desorption rate and incomplete desorption associated with impaired heating of bare SiO_2 relative to the temperatures achieved by NP-SiO_2 upon solar illumination. Thus, the net water harvesting capacity of the best-performing NP-SiO_2 was 25% greater than bare SiO_2 over a 12 hour period. As described above, with future innovation to limit NP-SiO_2 pore blockage attributed to APTES, NP-SiO_2 may achieve even greater improvements in water harvesting.

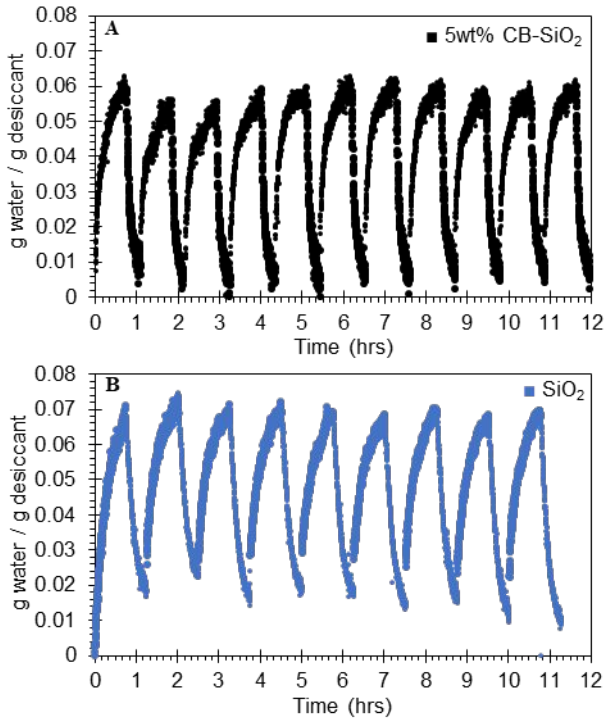

Figure 6: Experimental cycling of desiccants between adsorption at 40% RH and desorption under solar simulator. **A)** 5wt%CB-SiO_2 desiccants, adsorption performed for 45 minutes and

desorption performed for 20 minutes over 12 hours. **B)** SiO_2 desiccants, adsorption performed for 45 minutes and desorption performed for 30 minutes over 12 hours.

Theoretical atmospheric water capture potential by desiccants cycled in full-scale system

Figure 5B illustrates the theoretical water volume harvested over 12 hours by all desiccants under variable humidity conditions. In the most optimistic scenario, we assumed 12 hours of sunlight per day to drive water vapor desorption and use of highly-efficient condensation systems to recover water vapor desorbed from NP-SiO_2. The dual y-axes in **Figure 5B** show the mass of water captured *per gram of desiccant* over 12 hours (primary y-axis) and volume of water harvested by a likely full-scale system that contains a 10 mm thick layer of desiccants evenly coated over a 1 m^2 flat-bottomed AWC device (i.e., 4.5 kg of desiccant). The full-scale AWC system values represent a typical system configuration for passive AWC.[43] **Table S3** summarizes observed adsorption-desorption cycle time and the predicted number of cycles that can be achieved within 12 hours. At 40% RH, there is statistical ($p=0.035$) benefit to using a nano-enabled desiccant, with 2.1 ± 0.16 L/m^2 water harvested by 5wt%CB-SiO_2 compared to 1.7 ± 0.14 L/m^2 by bare SiO_2. NP-SiO_2 were able to produce more water over 12 hours because the cycle time is shorter and therefore more cycles can be performed.

At 60% and 80% RH conditions, all desiccants achieved similar water capture results. At 60% RH, even though all NP-SiO_2 can perform 3 more cycles than bare SiO_2, the total water volume was statistically similar ($p = 0.422$). Bare SiO_2 adsorbed 40% more water than NP-SiO_2, but also retained 40% of the adsorbed water vapor during desorption, leading to a net even water production by bare and nano-enabled desiccants. At 80% RH, total adsorption time was 6 hours for 5wt%AuNR-SiO_2 and 8 hours for all other desiccants, therefore only one adsorption and

desorption cycle can be performed over a 12 hour period. Water harvesting potential is then dictated by the capacity of a single cycle.

Future Outlook

We previously demonstrated the importance of geography and climate on the viability of performing passive desiccant driven AWC with solar-thermal water recovery.[43] Desiccant adsorption potential was a limiting factor in arid climates that had sufficient solar irradiance for desorption (e.g., southwest United States). Desiccant desorption potential was limiting in humid climates where there was insufficient solar irradiance to release the captured water (e.g., northwest, midwest and eastern United States). In this work, we found nano-enabled desiccants using silica coated with photothermal CB NPs are suitable in arid climates with abundant solar radiation (e.g., Phoenix, AZ) to capture water vapor from the air, even at low RH. NP-SiO_2 advance the state of science on solid desiccants for AWC, proving multiple cycles (>10) of adsorption and desorption can be performed within a 12 hour daylight period to maximize both adsorption and desorption potentials. A 5wt% CB-SiO_2 desiccant captured 0.562 g H_2O/g desiccant at 40% RH over 12 hours, an order of magnitude more than bare silica gel operated for only one cycle. Condensing the desorbed water can be achieved through heat exchange with cold air or a cold surface to bring the saturated water vapor to below dew point temperature.

A device to contain and operate the NP-SiO_2 must move beyond the traditional diurnal operation in batch configuration. Recently, Wang's group demonstrated a continuous atmospheric water generation device for photothermal liquid desiccant (nano carbon hollow capsule with hygroscopic salt LiCl inside the void core). Desiccants were contained on the surface of a rotating drum that moved between an adsorption zone open to ambient humid air and a desorption zone open to sunlight. A copper condensation chamber located above the desorption

zone condensed water droplets and directed them to a outlet.[53] A similar device can be constructed to hold and operate solid-phase photothermal desiccants in continuous mode throughout the day.

Acknowledgements

This work was funded through the National Science Foundation Nanosystems Engineering Research Center for Nanotechnology-Enabled Water Treatment (EEC-1449500) and National Science Foundation Graduate Research Fellowship. We acknowledge the use of facilities within the LeRoy Eyring Materials Center at Arizona State University. We thank Dr. Stephanie Loeb and Dr. Jaehong Kim for valuable insight in synthesis, characterization, and attachment of gold nanoparticles. Kaley Yazzie and Emma Westerhoff contributed to water capture and desiccant heating lab experiments. Laurel Passantino provided technical editing.

References

1 H. Stratton, H. Fuchs, Y. Chen, C. Dunham, C. C. Ni and A. Williams, Keeping Pace With Water and Wastewater Rates, *J. Am. Water Works Assoc.*, 2017, **109**, E426–E439.

2 B. Alspach and G. Juby, Cost-Effective ZLD Technology for Desalination Concentrate Management, *J. Am. Water Works Assoc.*, 2018, **110**, 37–47.

3 E. Jones, M. Qadir, M. T. H. Van Vliet, V. Smakhtin and S. Kang, The state of desalination and brine production : A global outlook, *Sci. Total Environ.*, 2019, **657**, 1343–1356.

4 T. A. Larsen, S. Hoffmann, C. Luthi, B. Truffer and M. Maurer, Emerging solutions to the

water challenges of an urbanizing world, *Science (80-.).*, 2016, **352**, 928–933.

5 United States Environmental Protection Agency, Small Drinking Water Systems Research, https://www.epa.gov/water-research/small-drinking-water-systems-research, (accessed 19 December 2019).

6 United States Environmental Protection Agency, Learn about Small Drinking Water Systems, https://www.epa.gov/dwcapacity/learn-about-small-drinking-water-systems, (accessed 19 December 2019).

7 E. A. Thomas, Ed., *Broken Pumps and Promises: Incentivizing Impact in Environmental Health*, Springer, 2016.

8 I. A. Shiklomanov, in *Water in crisis: a guide to the world's fresh water resources*, ed. P. H. Gleick, Oxford University Press, New York, 1992, pp. 13–24.

9 A. A. Salehi, M. Ghannadi-Maragheh, M. Torab-Mostaedi, R. Torkaman and M. Asadollahzadeh, A review on the water-energy nexus for drinking water production from humid air, *Renew. Sustain. Energy Rev.*, 2020, **120**, 109627.

10 R. V. Wahlgren, Atmospheric water vapour processor designs for potable water production: a review, *Water Res.*, 2001, **35**, 1–22.

11 D. Chen, J. Li, J. Zhao, J. Guo, S. Zhang, T. A. Sherazi, Ambreen and S. Li, Bioinspired superhydrophilic-hydrophobic integrated surface with conical pattern-shape for self-driven fog collection, *J. Colloid Interface Sci.*, 2018, **530**, 274–281.

12 K. C. Park, P. Kim, A. Grinthal, N. He, D. Fox, J. C. Weaver and J. Aizenberg,

Condensation on slippery asymmetric bumps, *Nature*, 2016, **531**, 78–82.

13 A. R. Parker and C. R. Lawrence, Water capture by a desert beetle, *Nature*, 2001, **414**, 33–34.

14 D. Li, J. Huang, G. Han and Z. Guo, A facile approach to achieve bioinspired PDMS@Fe 3 O 4 fabric with switchable wettability for liquid transport and water collection, *J. Mater. Chem. A*, 2018, **6**, 22741–22748.

15 B. T. W. Ang, J. Zhang, G. J. Lin, H. Wang, W. S. V. Lee and J. Xue, Enhancing Water Harvesting through the Cascading Effect, *ACS Appl. Mater. Interfaces*, 2019, **11**, 27464–27469.

16 B. S. Lalia, S. Anand, K. K. Varanasi and R. Hashaikeh, Fog-harvesting potential of lubricant-impregnated electrospun nanomats, *Langmuir*, 2013, **29**, 13081–13088.

17 US 2008/0314062 A1, 2008.

18 US 7.043.934 B2, 2006.

19 US 6,945,063 B2, 2005.

20 US 7,272,947 B2, 2007.

21 US 2010/0266742 A1, 2010.

22 US 5,669,221, 1997.

23 US 5,701,749, 1997.

24 US 6,343,479, 2002.

25 S. Misha, S. Mat, M. H. Ruslan and K. Sopian, Review of solid/liquid desiccant in the drying applications and its regeneration methods, *Renew. Sustain. Energy Rev.*, 2012, **16**, 4686–4707.

26 X. Zheng, T. S. Ge and R. Z. Wang, Recent progress on desiccant materials for solid desiccant cooling systems, *Energy*, 2014, **74**, 280–294.

27 P. A. Kallenberger and M. Fröba, Water harvesting from air with a hygroscopic salt in a hydrogel–derived matrix, *Commun. Chem.*, 2018, **1**, 28.

28 W. Wang, L. Wu, Z. Li, Y. Fang, J. Ding and J. Xiao, An Overview of Adsorbents in the Rotary Desiccant Dehumidifier for Air Dehumidification, *Dry. Technol.*, 2013, **31**, 1334–1345.

29 A. M. Hamed, Theoretical and experimental study on the transient adsorption characteristics of a vertical packed porous bed, *Renew. Energy*, 2002, **27**, 525–541.

30 M. M. Awad, A. Ramzy K, A. M. Hamed and M. M. Bekheit, Theoretical and experimental investigation on the radial flow desiccant dehumidification bed, *Appl. Therm. Eng.*, 2008, **28**, 75–85.

31 A. M. Hamed, W. R. Abd El Rahman and S. H. El-Eman, Experimental study of the transient adsorption/desorption characteristics of silica gel particles in fluidized bed, *Energy*, 2010, **35**, 2468–2483.

32 Y. C. Chiang, C. H. Chen, Y. C. Chiang and S. L. Chen, Circulating inclined fluidized

beds with application for desiccant dehumidification systems, *Appl. Energy*, 2016, **175**, 199–211.

33 N. Fumo and D. Y. Goswami, Study of an aqueous lithium chloride desiccant system: air dehumidification and desiccant regeneration, *Sol. Energy*, 2002, **72**, 351–361.

34 B. Gido, E. Friedler and D. M. Broday, Liquid-Desiccant Vapor Separation Reduces the Energy Requirements of Atmospheric Moisture Harvesting, *Environ. Sci. Technol.*, 2016, **50**, 8362–8367.

35 S. Jain and P. K. Bansal, Performance analysis of liquid desiccant dehumidification systems, *Int. J. Refrig.*, 2007, **30**, 861–872.

36 V. Martin and D. . Goswami, Heat and Mass Transfer in Packed Bed Liquid Desiccant Regenerators—An Experimental Investigatio, *Sol. Energy Energy Conserv.*, 1999, **121**, 162–170.

37 V. Öberg and D. Y. Goswami, Experimental Study of the Heat and Mass Transfer in a Packed Bed Liquid Desiccant Air Dehumidifier, *J. Sol. Energy Eng.*, 1998, **120**, 289.

38 R. Li, Y. Shi, L. Shi, M. Alsaedi and P. Wang, Harvesting Water from Air: Using Anhydrous Salt with Sunlight, *Environ. Sci. Technol.*, 2018, **52**, 5398–5406.

39 A. P. Cohen, in *Kirk-Othmer Encyclopedia of Chemical Technology*, John Wiley & Sons, Inc., Hoboken, NJ, USA, 2003.

40 A. Lapotin, H. Kim, S. R. Rao and E. N. Wang, Adsorption-Based Atmospheric Water Harvesting: Impact of Material and Component Properties on System-Level Performance,

Acc. Chem. Res., 2019, **52**, 1588–1597.

41 H. Kim, S. Yang, S. R. Rao, S. Narayanan, E. A. Kapustin, H. Furukawa, A. S. Umans, O. M. Yaghi and E. N. Wang, Water harvesting from air with metal-organic frameworks powered by natural sunlight, *Science (80-.).*, 2017, **356**, 430–434.

42 H. Kim, S. R. Rao, E. A. Kapustin, L. Zhao, S. Yang, O. M. Yaghi and E. N. Wang, Adsorption-based atmospheric water harvesting device for arid climates, *Nat. Commun.*, 2018, **9**, 1–8.

43 A. Mulchandani and P. Westerhoff, Geospatial Climatic Factors Influence Water Production of Solar Desiccant Driven Atmospheric Water Capture Devices, *Environ. Sci. Technol.*, 2020, **54**, 8310–8322.

44 US 2018/0043295 A1, 2018.

45 H. Kim, S. R. Rao, E. A. Kapustin, L. Zhao, S. Yang, O. M. Yaghi and E. N. Wang, Adsorption-based atmospheric water harvesting device for arid climates, *Nat. Commun.*, 2018, **9**, 1–8.

46 F. Fathieh, M. J. Kalmutzki, E. A. Kapustin, P. J. Waller, J. Yang and O. M. Yaghi, Practical water production from desert air, *Sci. Adv.*, 2018, **4**, eaat3198.

47 J. Yan, Y. Yu, C. Ma, J. Xiao, Q. Xia, Y. Li and Z. Li, Adsorption isotherms and kinetics of water vapor on novel adsorbents MIL-101(Cr)@GO with super-high capacity, *Appl. Therm. Eng.*, 2015, **84**, 118–125.

48 A. Khutia, H. U. Rammelberg, T. Schmidt, S. Henninger and C. Janiak, Water Sorption

Cycle Measurements on Functionalized MIL-101Cr for Heat Transformation Application, *Chem. Mater.*, 2013, **25**, 790–798.

49 G. Akiyama, R. Matsuda, H. Sato, A. Hori, M. Takata and S. Kitagawa, Effect of functional groups in MIL-101 on water sorption behavior, *Microporous Mesoporous Mater.*, 2012, **157**, 89–93.

50 P. D. Dongare, A. Alabastri, S. Pedersen, K. R. Zodrow, N. J. Hogan, O. Neumann, J. Wu, T. Wang, A. Deshmukh, M. Elimelech, Q. Li, P. Nordlander and N. J. Halas, Nanophotonics-enabled solar membrane distillation for off-grid water purification., *Proc. Natl. Acad. Sci. U. S. A.*, 2017, **114**, 6936–6941.

51 S. Loeb, C. Li and J. H. Kim, Solar Photothermal Disinfection using Broadband-Light Absorbing Gold Nanoparticles and Carbon Black, *Environ. Sci. Technol.*, 2018, **52**, 205–213.

52 R. Li, Y. Shi, M. Alsaedi, M. Wu, L. Shi and P. Wang, Hybrid Hydrogel with High Water Vapor Harvesting Capacity for Deployable Solar-Driven Atmospheric Water Generator, *Environ. Sci. Technol.*, 2018, **52**, 11367–11377.

53 R. Li, Y. Shi, M. Wu, S. Hong and P. Wang, Improving atmospheric water production yield: Enabling multiple water harvesting cycles with nano sorbent, *Nano Energy*, 2020, **67**, 104255.

54 J. Qiu and W. D. Wei, Surface Plasmon-Mediated Photothermal Chemistry, *J. Phys. Chem. C*, 2014, **118**, 20735–20749.

55 R. D. Averitt, S. L. Westcott and N. J. Halas, Linear optical properties of gold nanoshells, *J. Opt. Soc. Am. B*, 1999, **16**, 1824.

56 H. H. Richardson, M. T. Carlson, P. J. Tandler, P. Hernandez and A. O. Govorov, Experimental and theoretical studies of light-to-heat conversion and collective heating effects in metal nanoparticle solution, *Nano Lett.*, 2009, **9**, 1139–1146.

57 P. Wang, Emerging investigator series: the rise of nano-enabled photothermal materials for water evaporation and clean water production by sunlight, *Environ. Sci. Nano*, 2018, **5**, 1078–1089.

58 A. O. Govorov and H. H. Richardson, Generating heat with metal nanoparticles, *Nano Today*, 2007, **2**, 30–38.

59 D. K. Roper, W. Ahn and M. Hoepfner, Microscale Heat Transfer Transduced by Surface Plasmon Resonant Gold Nanoparticles, *J. Phys. Chem. C*, 2007, **111**, 3636–3641.

60 R. Jiang, S. Cheng, L. Shao, Q. Ruan and J. Wang, Mass-based photothermal comparison among gold nanocrystals, PbS nanocrystals, organic dyes, and carbon black, *J. Phys. Chem. C*, 2013, **117**, 8909–8915.

61 S. C. Nguyen, Q. Zhang, K. Manthiram, X. Ye, J. P. Lomont, C. B. Harris, H. Weller and A. P. Alivisatos, Study of Heat Transfer Dynamics from Gold Nanorods to the Environment via Time-Resolved Infrared Spectroscopy, *ACS Nano*, 2016, **10**, 2144–2151.

62 O. Neumann, A. S. Urban, J. Day, S. Lal, P. Nordlander and N. J. Halas, Solar vapor generation enabled by nanoparticles, *ACS Nano*, 2013, **7**, 42–49.

63 D. Han, Z. Meng, D. Wu, C. Zhang and H. Zhu, Thermal properties of carbon black aqueous nanofluids for solar absorption, *Nanoscale Res. Lett.*, 2011, **6**, 457.

64 Y. Wang and L. Tang, Chemisorption Assembly of Au Nanorods on Mercaptosilanized Glass Substrate for Label-free Nanoplasmon Biochip, *Anal. Chim. Acta*, , DOI:10.1016./j.aca.2013.08.024.

65 J. A. Bae, K.-C. Song, J.-K. Jeon, Y. S. Ko, Y.-K. Park and J.-H. Yim, Effect of pore structure of amine-functionalized mesoporous silica-supported rhodium catalysts on 1-octene hydroformylation, *Microporous Mesoporous Mater.*, 2009, **123**, 289–297.

66 X. Liu, A. Wang, X. Yang, T. Zhang, C. Y. Mou, D. S. Su and J. Li, Synthesis of thermally stable and highly active bimetallic Au-Ag nanoparticles on inert supports, *Chem. Mater.*, 2009, **21**, 410–418.

67 B. E. Brinson, J. B. Lassiter, C. S. Levin, R. Bardhan, N. Mirin and N. J. Halas, in *Langmuir*, 2008, vol. 24, pp. 14166–14171.

68 N. Aissaoui, L. Bergaoui, J. Landoulsi, J.-F. Lambert and S. Boujday, Silane Layers on Silicon Surfaces: Mechanism of Interaction, Stability, and Influence on Protein Adsorption, *Langmuir*, 2012, **28**, 656–665.

69 X. Rao, C. Guyon, S. Ognier, B. Da Silva, C. Chu, M. Tatoulian and A. A. Hassan, High density gold nanoparticles immobilized on surface via plasma deposited APTES film for decomposing organic compounds in microchannels, *Appl. Surf. Sci.*, 2018, **439**, 272–281.

70 K. Greben, P. Li, D. Mayer, A. Offenhäusser and R. Wördenweber, Immobilization and

surface functionalization of gold nanoparticles monitored via streaming current/potential measurements, *J. Phys. Chem. B*, 2015, **119**, 5988–5994.

71 H. H. Kyaw, S. H. Al-Harthi, A. Sellai and J. Dutta, Self-organization of gold nanoparticles on silanated surfaces, *Beilstein J. Nanotechnol.*, 2015, **6**, 2345–2353.

72 M. Ben Haddada, J. Blanchard, S. Casale, J. M. Krafft, A. Vallée, C. Méthivier and S. Boujday, Optimizing the immobilization of gold nanoparticles on functionalized silicon surfaces: Amine- vs thiol-terminated silane, *Gold Bull.*, 2013, **46**, 335–341.

73 V. V. Apyari, V. V. Arkhipova, M. V. Gorbunova, P. A. Volkov, A. I. Isachenko, S. G. Dmitrienko and Y. A. Zolotov, Towards the development of solid-state platform optical sensors: aggregation of gold nanoparticles on polyurethane foam, *Talanta*, 2016, **161**, 780–788.

74 X. Huang, X. Liao and B. Shi, Synthesis of highly active and reusable supported gold nanoparticles and their catalytic applications to 4-nitrophenol reduction, *Green Chem.*, 2011, **13**, 2801–2805.

75 H. G. Hecht, The Interpretation of Diffuse Reflectance Spectra, *J. Res. NBS A Phys. Ch.*, 1976, **80**, 567–583.

76 S. Linden, J. Kuhl and H. Giessen, Controlling the interaction between light and gold nanoparticles: Selective suppression of extinction, *Phys. Rev. Lett.*, 2001, **86**, 4688–4691.

77 C. Sönnichsen, T. Franzl, T. Wilk, G. von Plessen, J. Feldmann, O. Wilson and P. Mulvaney, Drastic reduction of plasmon damping in gold nanorods, *Phys. Rev. Lett.*,

2002, **88**, 774021–774024.

78 J. J. Mock, D. R. Smith and S. Schultz, Local refractive index dependence of plasmon resonance spectra from individual nanoparticles, *Nano Lett.*, 2003, **3**, 485–491.

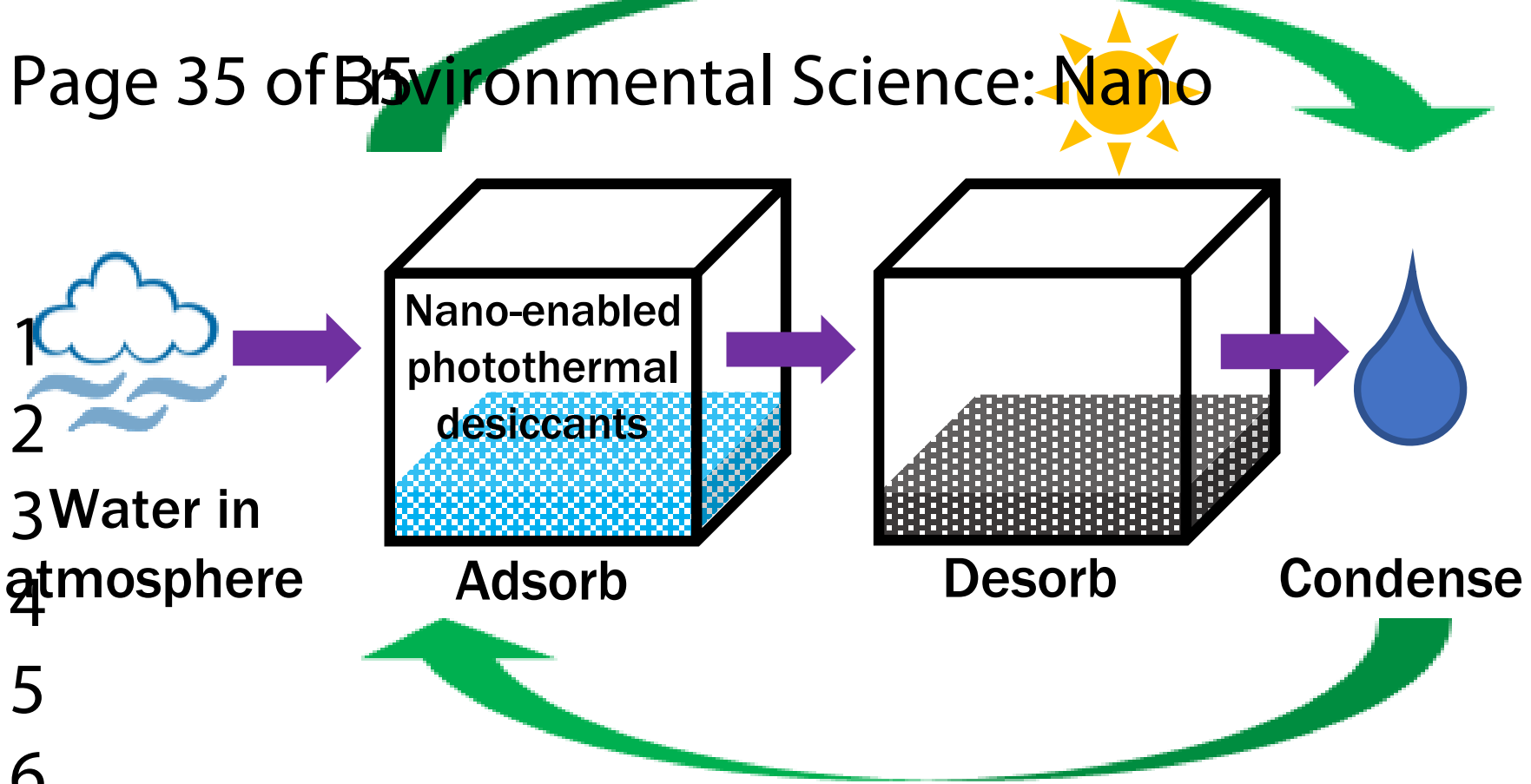
Nano-enabled
photothermal
desiccants
Water in
atmosphere
Adsorb
Desorb
Condense